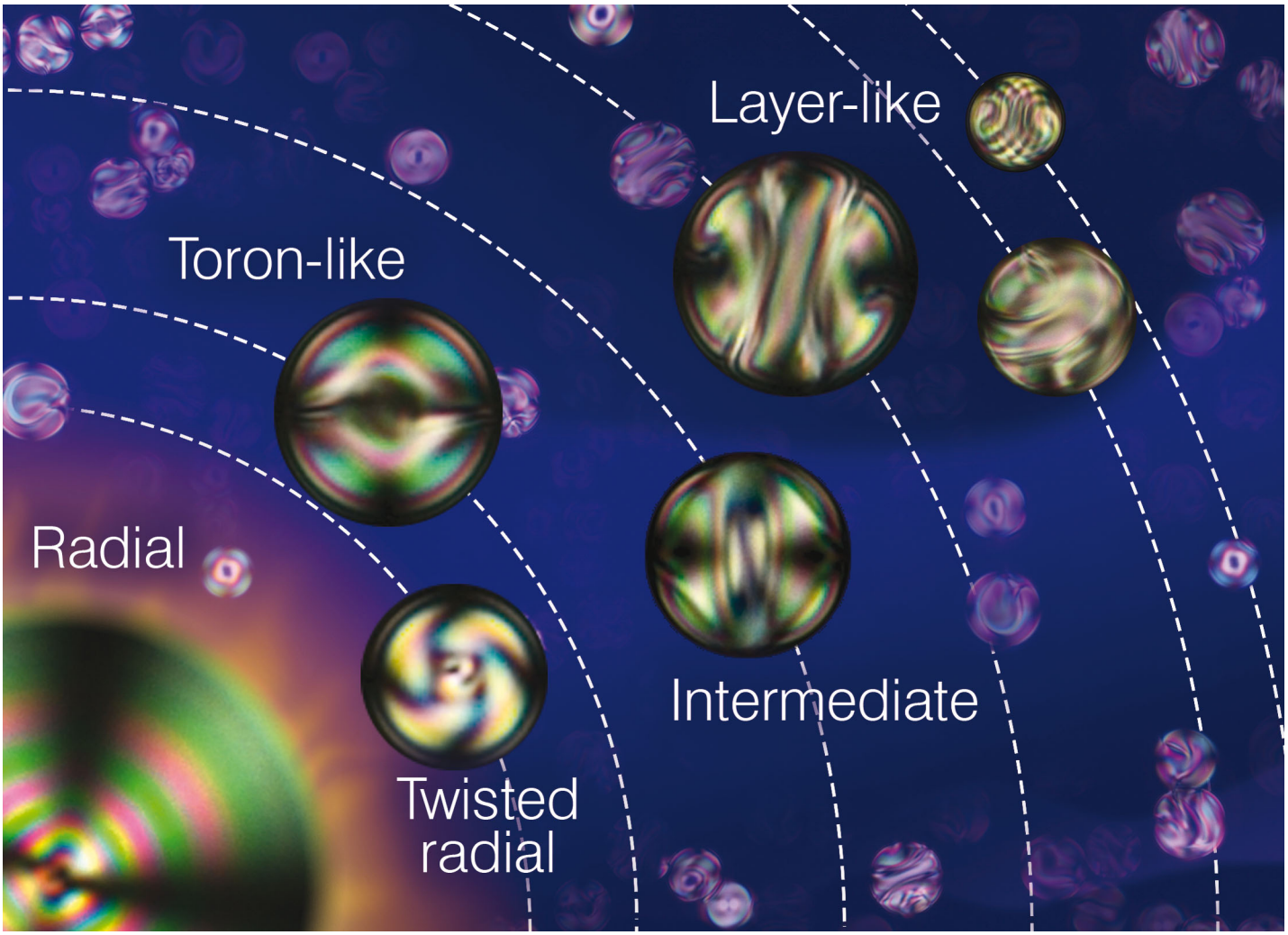

Highlighting research from the collaboration between Kirensky Institute of Physics, SB RAS, Krasnoyarsk, Russia, and Lomonosov Moscow State University, Russia.

Orientational structures in cholesteric droplets with homeotropic surface anchoring

Cholesteric droplets show high diversity of stable and metastable structures. We study this phenomenon by combining experimental techniques with computer simulations. Advanced lattice Monte Carlo methods allow us to discover and identify a great variety of structures in simulations, as well as match the data with the experimental findings on a quantitative level.

As featured in:

See Vladimir Yu. Rudyak *et al.*, *Soft Matter*, 2019, **15**, 5554.

ROYAL SOCIETY OF CHEMISTRY | Celebrating IYPT 2019

rsc.li/soft-matter-journal

Registered charity number: 207890

Soft Matter

PAPER

View Article Online
View Journal | View Issue

Cite this: *Soft Matter*, 2019, **15**, 5554

Orientational structures in cholesteric droplets with homeotropic surface anchoring†

Mikhail N. Krakhalev,[ab] Vladimir Yu. Rudyak,*[c] Oxana O. Prishchepa,[ab] Anna P. Gardymova,[b] Alexander V. Emelyanenko,[c] Jui-Hsiang Liu[d] and Victor Ya. Zyryanov[a]

Received 21st February 2019,
Accepted 17th June 2019

DOI: 10.1039/c9sm00384c

rsc.li/soft-matter-journal

The dependency of orientational structures in cholesteric droplets with homeotropic surface anchoring on the helicity parameter has been studied by experiment and simulations. We have observed a sequence of structures, in which the director configurations and topological defects were identified by comparison of polarized microscopy pictures with simulated textures. A toron-like and low-symmetry intermediate layer-like structures have been revealed and studied in detail. The ranges of stability of the observed structures have been summarized in a general diagram and explained by the helicity parameter dependence of the free energy terms.

1 Introduction

Cholesteric liquid crystals (CLC) are unique soft matter objects due to their ability to form structure diversity.[1] Recent studies on CLC boasts deep insights it produced in many areas such as biosensors,[2] display technologies,[3] and other applications.[4] The direct connection between topological defects in particle physics and liquid crystals[5] allows to use liquid crystals as convenient systems for studies of several fundamental problems.[6,7] Even more intriguing, CLC phases are often formed by biological building blocks, such as DNA and viruses.[8] Since the packing and thus functioning of these molecules is highly affected by the geometrical constraints of the bounding space, the studies of CLC in confined geometries became very important.[9,10]

The diversity of structures in them is caused by the incompatibility of the equilibrium helicoidal structure of the cholesteric and confinement of the droplet. Under the action of the bounding surfaces, the helicoidal structure is deformed and various orientational structures of the cholesteric are formed depending on the material parameters of the CLC, the boundary conditions and the ratio of the intrinsic helix pitch p_0 and the layer thickness h. For example, at the lower h/p_0 ratio the cholesteric helix is untwisted completely and a nematic structure occurs.[11–13] At h/p_0 exceeding one, various periodical structures appear in correspondence with the boundary conditions[11,14–19] and applied electric (magnetic) field.[20,21] In spherical droplets with homeotropic anchoring, various orientational structures with singular or nonsingular topological defects are formed. At $h/p_0 \approx 1$, cholesteric spherulites, fingers,[22–26] other solitons[7,27–29] and periodic structures based on them[30–33] arise.

In droplet dispersions, CLC are embedded into closed cavities, which influence considerably their optical,[34–37] optomechanical,[37,38] thermo-mechanical[39,40] and hydrodynamic properties.[41] The structures formed depend also on the boundary conditions and on the ratio of the intrinsic helix pitch to the cavity size. For instance, under tangential anchoring various droplet structures are found: twisted bipolar configurations,[42–44] structures with χ^{+2} dislocation or topologically equivalent double-helix/two χ^{+1} disclinations,[42,43,45–48] structures with diametrical χ^{+1} dislocation or topologically equivalent configurations with pairs of +1/2 and +3/2 linear defects or a set of pairs of +1/2 and −1/2 circular defects.[43,45,47,49] The bipolar configuration is formed at relatively large helix pitch. At smaller helix pitch, the structure transforms into the configuration with χ^{+2} dislocation.[42,44]

Homeotropic anchoring at the droplets' boundary also allows many different structures to exist: ones with combinations of point defects in the bulk and near the surface,[50–52] structures with a bipolar distribution of the cholesteric helix,[45,53,54] "nested cups" structures[45] and other layer-like structures[55,56] depending on the relative helicity parameter $N_0 = 2d/p_0$ (d is a droplet diameter). It should be noted that the pitch p observed in cholesteric droplets with homeotropic anchoring can be significantly different from the intrinsic helix pitch p_0. This distinction

[a] *Kirensky Institute of Physics, Federal Research Center – Krasnoyarsk Scientific Center, Siberian Branch, Russian Academy of Sciences, Krasnoyarsk 660036, Russia*
[b] *Institute of Engineering Physics and Radio Electronics, Siberian Federal University, Krasnoyarsk 660041, Russia*
[c] *Faculty of Physics, Lomonosov Moscow State University, Moscow, 119991, Russia. E-mail: vurdizm@gmail.com*
[d] *National Cheng Kung University, Tainan 70101, Taiwan*

† Electronic supplementary information (ESI) available: (I) Analysis of discretization effects in simulations. (II) The spectrum of the microscope halogen lamp. (III) Droplet with the intermediate structure. (IV) Four structures observed in droplets with $4.7 \leq N_0 \leq 5.5$. See DOI: 10.1039/c9sm00384c

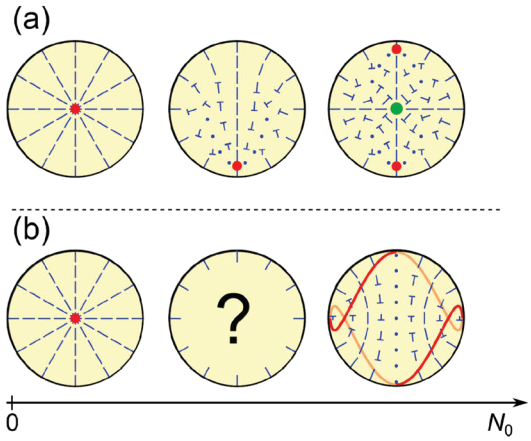

Fig. 1 Director configuration sequences at different relative helicity parameter $N_0 = 2d/p_0$ in CLC droplets formed by cooling of the cholesteric from its isotropic phase (a) and by phase separation methods within a polymer matrix (b). The boundary conditions are homeotropic in both (a and b).

caused by the unwinding effect was studied in detail in ref. 57. Therefore, the pitch p in cholesteric droplets under study can be twice or more than the intrinsic helix pitch p_0. Consequently, the value of N_0 exceeds the chirality parameter $N = 2d/p$ determined using experimental optical textures of the droplets. At low N_0, structures with point defects are observed in the droplets on cooling of CLC from the isotropic phase. Formation of such defects allows the homeotropic orientation to remain over the whole droplet surface with simultaneous realization of an intricate pattern of director twisting in the bulk. The larger N_0 the larger the number of defects (Fig. 1a) in the droplet, with the total topological charge of defects remaining +1.[50,51] Under relatively large N_0 layer-like structures are observed more often, for example, with a bipolar distribution of the helical axis.[45,54,55] In this case, a twisted loop defect appears near the droplet surface.[54] It allows the homeotropic orientation of the director to remain almost over the whole droplet surface, and simultaneously the director field twists in the bulk.

CLC structures with several point defects were observed in ref. 51 and structures with a bipolar distribution of the helical axis containing a twisted loop defect were found for the droplets with the same N_0.[54] As a consequence, various sets of configurations depending on the N_0 number can be formed in different systems. In the case of structures with point defects obtained by cooling of CLC from the isotropic phase, this sequence can be presented as follows: the untwisted radial configuration – twisted structure with a shifted point defect – structure with three point defects and so on[51] (Fig. 1a). The droplets studied in ref. 54 were dispersed in a polymer by the phase separation method. These droplets formed in the growing process are in the liquid crystal phase (at least, at the final stage). It can result in another dependence of observable CLC structures on N_0 (Fig. 1b). However, structures intermediate between the radial configuration and layer-like structures with linear defects have not been considered up to now. In the present paper the orientation structures of CLC droplets in a polymer with homeotropic anchoring have been studied for various values of the helicity parameter in the $0 < N_0 \leq 7$ range.

2 Methods

2.1 Experimental

Films of polymer dispersed chiral nematic liquid crystals (PDCLC) based on poly(isobutyl methacrylate) (PiBMA) (Sigma) and the E7 nematic (Merck) doped with a cholesteryl acetate (Ch) chiral dopant have been studied. The weight ratio of the CLC components was E7 : Ch = 97 : 3. The intrinsic helix pitch of the CLC p_0 equals 5.5 μm.[57] The PDCLC films were made by the SIPS (solvent induced phase separation) method.[58] 35 μm thickness PDCLC films with CLC droplets of 5–30 μm diameter in the film plane were obtained. The optical textures of the chiral nematic droplets were examined using a polarizing optical microscope Axio Imager.A1m (Carl Zeiss) with a 50× objective.

2.2 Computer simulations

2.2.1 Calculations of the droplet structure. We performed calculations of the LC structure within a spherical cavity filled with chiral nematic. The cavity was rendered in a 48 × 48 × 48 lattice (see Fig. S1–S6 (ESI†) for details on discretization effects; the estimated error in the position of transition points due to discretization is ~2%). We used the extended Frank elastic continuum approach with Monte-Carlo annealing optimization[59] to find energy-optimal droplet structures. This has previously shown good results for nematic and cholesteric LC.[54,60,61] This approach includes the effects of the director field distortion and the formation of defects in the droplet:

$$F = \int_V \left(\frac{K_{11}}{2}(\mathrm{div}\mathbf{n})^2 + \frac{K_{22}}{2}(\mathbf{n}\cdot\mathrm{rot}\mathbf{n} + q_0)^2 + \frac{K_{33}}{2}[\mathbf{n}\times\mathrm{rot}\mathbf{n}]^2 \right) \mathrm{d}V + \frac{W}{2}\int_\Omega \left[1 - \cos^2\gamma\right]\mathrm{d}\Omega + F_{\mathrm{def}}, \quad (1)$$

where K_{11}, K_{22} and K_{33} are the splay, twist and bend elasticity constants, respectively, W is the surface anchoring energy density, γ is the angle between the local director and the normal to the droplet surface, and F_{def} is the energy of defects calculated by summation of the point and linear defect energies. The types, positions and energies of defects were estimated automatically during the Monte-Carlo optimization procedure (see the details in ref. 59). The ratio between elasticity constants was set to $K_{11} : K_{22} : K_{33} = 1 : 0.6 : 1.25$ to simulate the cholesteric liquid crystal mixture under study. The linear energy density of the disclination core was set to $f_{\mathrm{core}}^{\mathrm{line}} = 2.75K_{11}$, and the anchoring strength $\mu = WR/K_{11} = 200$ was used for simulation of strong anchoring. Here R is the radius of the droplet. The equilibrium cholesteric pitch was set to $p_0 = 2\pi/q_0 = 5.5$ μm.

2.2.2 Calculation of the droplet picture in crossed polarizers. We have calculated the droplet textures using the Jones matrices technique, formulated for PDLC materials in ref. 62. This technique supposes direct unidirectional propagation of linearly polarized light through a non-uniform birefringent material. Light diffraction, diffusion and scattering are not taken into account in Jones calculus, and thus the textures on the peripheral parts of the

droplets are roughly estimated. The textures were calculated for ten different wavelengths within the visible spectrum, from 400 nm to 700 nm with equal steps of 33 nm. The values of ordinary and extraordinary refractive indices for the E7 nematic were set dependent on the wavelength in correspondence with ref. 63. The color textures were generated by merging the individual wavelength textures with regard to the experimental halogen lamp intensity at each wavelength (see Fig. S9, ESI†).

3 Results and discussion

3.1 Structures with point defects

The well-known radial (**R**) structure[64] is observed in the smallest droplets up to a size of 3 μm (corresponds to $N_0 = 1.1$). The point defect is located in the droplet center, and the director distribution is untwisted. This structure has the highest possible symmetry for the described system, $D_{\infty h}$.

In the droplets larger than $N_0 = 1.1$, the twisted radial (**tR**) structure is observed. It still contains only one point defect, but it is sufficiently shifted toward the edge of the droplet. At $N_0 = 1.8$ ($d = 5$ μm) this defect lies almost at the edge of the droplet, and does not move with a further increase in the size of the droplet. Simultaneously, the high overall twist of the director field compensates the twisting power of the CLC (see Fig. 2), which is visualized by the extinction lines of the radial structure. The resulting structure corresponds to C_∞ symmetry.

3.2 Toron-like structure

The toron-like structure (**T**) is observed in the medium-sized droplets (with a diameter within the range from 8 to 16 μm, corresponding to $2.9 \leq N_0 \leq 5.8$). This highly-symmetrical structure (D_∞) causes the formation of an equatorial circular defect line near the surface of the droplet (see Fig. 3). The defect is clearly seen when the symmetry axis of the structure is in the film plane (Fig. 3, top row). Minor distortions of the circular defect appear in the droplets with diameter $d < 10$ μm. The director field twists in the cross-section normal to the symmetry axis. In the droplets with diameter $d > 10$ μm ($N_0 > 3.6$), the simulated structures correspond to a total twist angle equal to π, independently of the droplet size. It is confirmed by the absence of additional lines in the optical textures in cross-polarized microphotographs (Fig. 3, bottom row).

3.3 Layer-like structures

A further increase of the droplet diameter stabilizes layer-like (**L**) structures with a bipolar distribution of helical axes and with a double twist defect line near the surface.[54] The distinguishing feature of the system studied is bistability in layer-like structures. The layer-like structure with a small twist defect is stable in droplets with a diameter from 12 to 16 μm (Fig. 4).

The central part of the corresponding texture has a narrow band along the *x*-axis, with the director oriented along the view axis. The circular defect in this structure is deformed sufficiently and intersects the equatorial plane at the four points (see details in Fig. S10, ESI†). The number of twists *N* in this structure is approximately 1.8 and does not change with the droplet size. Thus we will call it the intermediate layer-like structure and denote it as $\mathbf{L}_0$ to indicate both its fixed geometry and layer-like nature.

The projection of the circular defect on the other principal cross-section forms a figure-of-eight (see Fig. 4, bottom row and Fig. S11 for details, ESI†). It is accompanied by an increased edge-to-edge director twist, which is clearly seen in the interference texture in cross-polarizers (Fig. 4c).

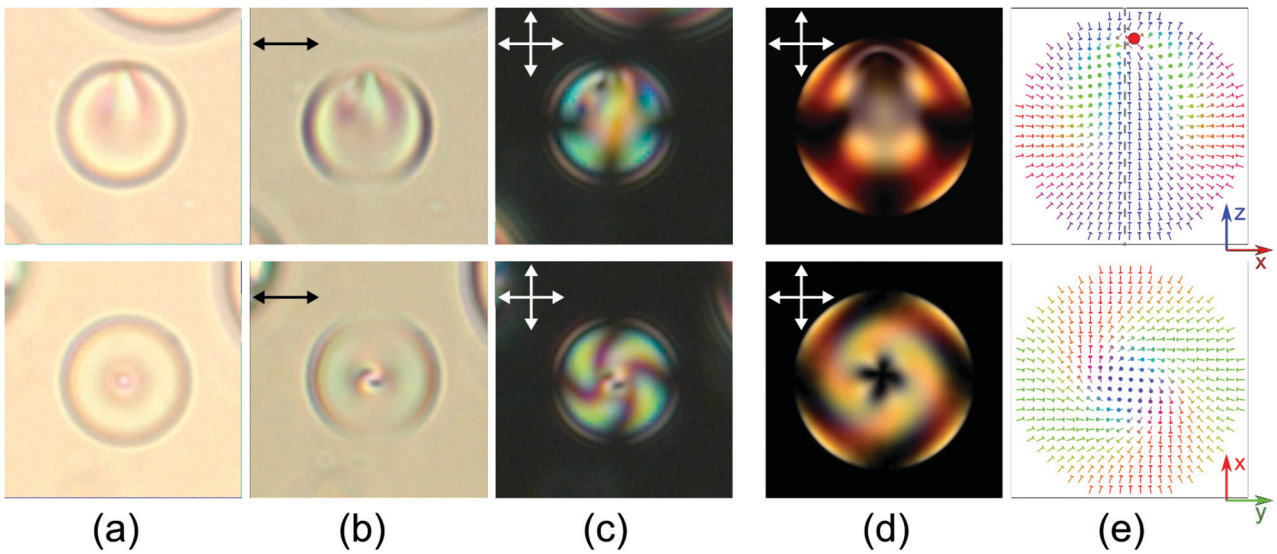

Fig. 2 Optical textures and director distributions of a 7.5 μm droplets ($N_0 = 2.7$) having the twisted radial (**tR**) structure. Microphotographs are taken in unpolarized light (a), at without analyzer (b), and in crossed polarizers (c). The simulated cross-polarized images (d) and corresponding director distributions in the central cross-section (e). The symmetry axis is oriented parallel (top row) and perpendicular (bottom row) to the viewing plane. Hereinafter, double arrows indicate the direction of the polarizers, and the director **n** in (e) is colored in correspondence with the direction (red along the *x*-axis, green along the *y*-axis, blue along the *z*-axis), and the nail tops mark an out-of-plane heading. The thick red point shows the location of a point bulk defect.

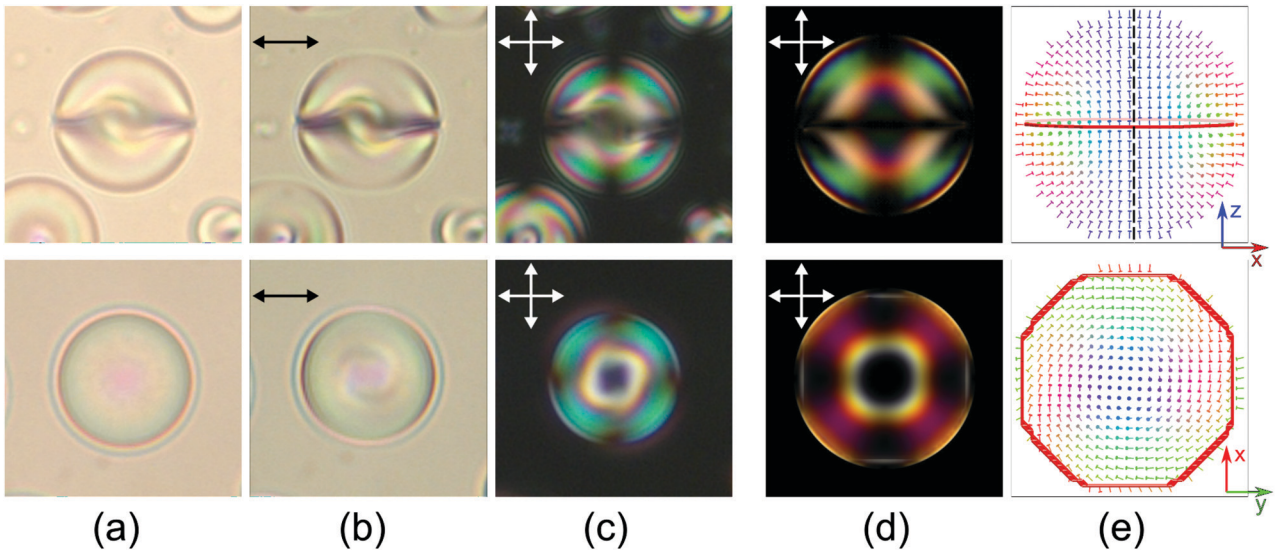

Fig. 3 Optical textures and director distributions of a 14 μm droplets (N_0 = 5.1) having the toron-like (**T**) structure. Microphotographs are taken in unpolarized light (a), at without analyzer (b), and in crossed polarizers (c). The simulated cross-polarized images (d) and corresponding director distributions in the central cross-section (e). The symmetry axis is oriented parallel (top row) and perpendicular (bottom row) to the viewing plane. The thick red line indicates the circular linear defect near the surface.

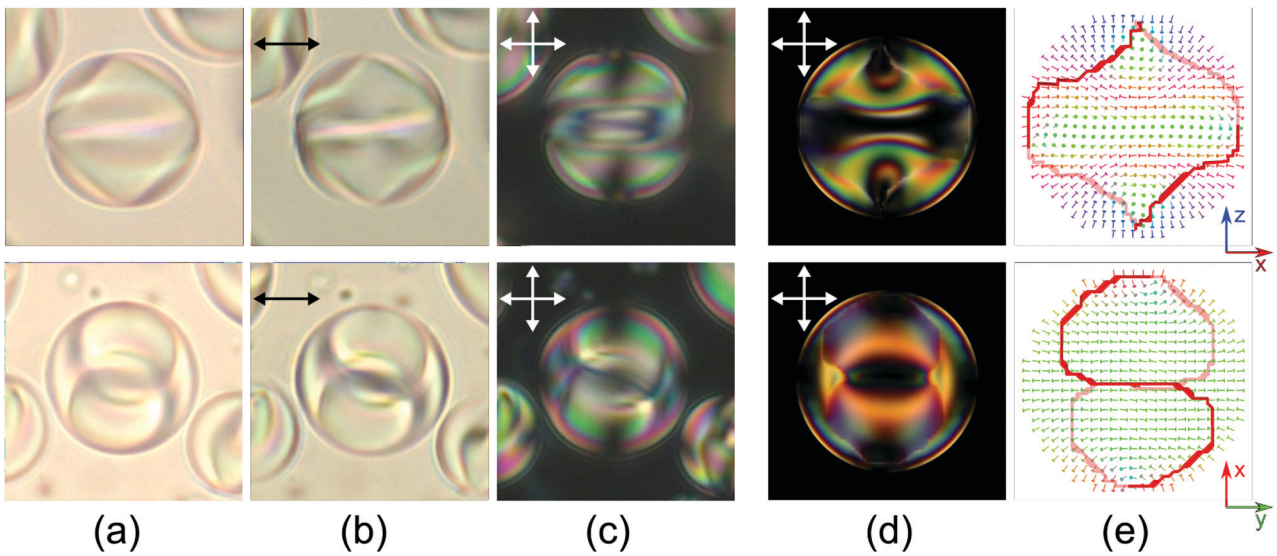

Fig. 4 Optical textures and director distributions of a 15 μm droplets (N_0 = 5.5) having the intermediate ($\mathbf{L}_0$) structure. Microphotographs are taken in unpolarized light (a), at without analyzer (b), and in crossed polarizers (c). The simulated cross-polarized images (d) and corresponding director distributions in the central cross-section (e). The line of the distorted defect primarily lies in the plane of the film (top row) and perpendicular to it (bottom row). The thick red line indicates the twisted loop defect near the surface (hereinafter the shaded red defect lines are beyond the image plane, and the solid lines are above it).

We should pay attention to a minor change of the optical pattern color of the droplet with the **T** structure. It is explained by the fact that in the **T** structure the effective Δn, which is equal to zero in the droplet center, gradually increases toward the droplet edges due to the turn of the director with respect to the view direction. At the same time, the thickness of the LC layer diminishes along the radius near the droplet border. The influences of these two effects with respect to the phase difference between ordinary and extraordinary rays compensate each other and, consequently, the color of the droplet texture changes insignificantly. A richer color gamut is observed in the droplet optical texture of the layer-like intermediate structure ($\mathbf{L}_0$) at the same droplet size (see Fig. S11, ESI†). It means that the director turns at a greater angle along the droplet diameter in comparison with that in the toron-like configuration. On the other hand, comparing the optical texture of the intermediate structure and normal layer-like structure (Fig. S11c and d, ESI†), one concludes that the lensing effect in the intermediate

structure is insignificant. It means that the smaller gradient of the refractive index along the film plane is caused by the smaller twist of the director, and corresponds to a number of π turns along the bipolar axis $N \cong 1.8$ of the structure (Fig. S11d, ESI†).[54]

A further increase of the droplet diameter stabilizes the layer-like (**L**) structures with a bipolar distribution of helical axes and with a regular double twist defect line near the surface (see Fig. 5).[54] These structures are observed at a droplet diameter of 13 μm and larger ($N_0 \geq 4.7$). The number of director π turns continuously rises with the increasing size of the droplet in the layer-like structures.[57]

The stability of the two types of layer-like structures, $\mathbf{L}_0$ and **L**, is explained by the bistability of the layer-like structure in the region of smaller droplet diameters. The balance between elastic and defect energies results in two energy minima ($\mathbf{L}_0$ and **L**) in between $N_0 = 5.2$ and 5.8 (see details in Section "$\mathbf{L}_0$–**L** transition"). These minima are separated by an energy barrier, making it unfavorable for $\mathbf{L}_0$ to transform to the regular **L** structure by further twisting.

3.4 Diagram of states and stability of the structures

The measured and calculated diagrams of states are presented in Fig. 6. Both demonstrate the same sequence of states with increasing helicity parameter N_0: radial (**R**) – twisted radial (**tR**) – toron-like (**T**) – intermediate layer-like ($\mathbf{L}_0$) – layer-like (**L**) structures.

In the experiment, the radial structure with no twist prevails up to $N_0 = 1.1$, which is two times smaller than the threshold value for $N_{th} = 2h/p_0 \cong 2.5$,[12] calculated for the E7 liquid crystal. Larger droplets demonstrate a variety of structures, with greater complexity and director field distortion with the increasing size of the droplet. Notably, the stability ranges of various structure kinds correlate nicely in theory and experiment (Fig. 6(a)). A single stable structure is obtained for droplets below $N_0 = 2.9$. Droplets in the range of $2.9 \leq N_0 \leq 4.4$ can form both twisted radial and toron-like states. In the range of $4.4 \leq N_0 \leq 4.7$, droplets with intermediate structure can be found as well. Notably, droplets between $N_0 = 4.7$ and 5.4 can form four different structures (**tR**, **T**, $\mathbf{L}_0$ and **L**) under equal conditions. The twisted radial configuration becomes unstable at $N_0 > 5.4$, and droplets larger than $N_0 = 5.8$ demonstrate only the layer-like structure.

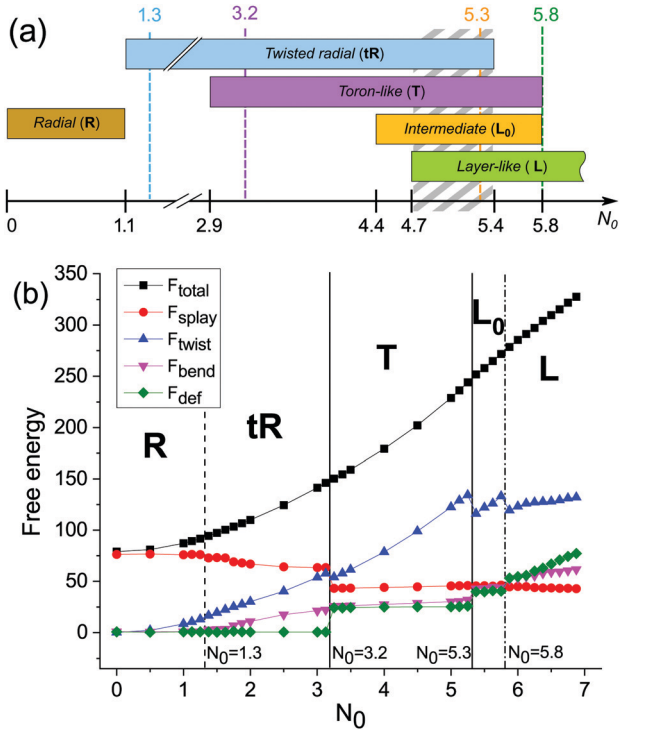

Fig. 6 (a) Diagram of the droplet state observed experimentally at various droplet sizes expressed by the relative helicity parameter N_0. The range of coexistence of the four structures is shown with grey hatch. Colored vertical lines indicate positions of the structure transitions obtained in calculations (below). (b) Dependence of the free energy, and its elastic and surface terms on the droplet size. The dashed vertical line indicates the second order structure transition, and the solid and dash-dot vertical lines indicate the first order structure transitions.

The results of computer simulations are summarized in Fig. 6(b). At each helicity parameter, only the structures with the lowest free energy were taken into account for the following analysis (see Section 2). Thus, the ranges of stability of different structures in the diagram of states do not overlap. At the same time, as shown below, detailed analysis of the evaluation of various terms of the free energy with increasing N_0 demonstrates the four structure transitions in the system explaining the experimental diagram of states.

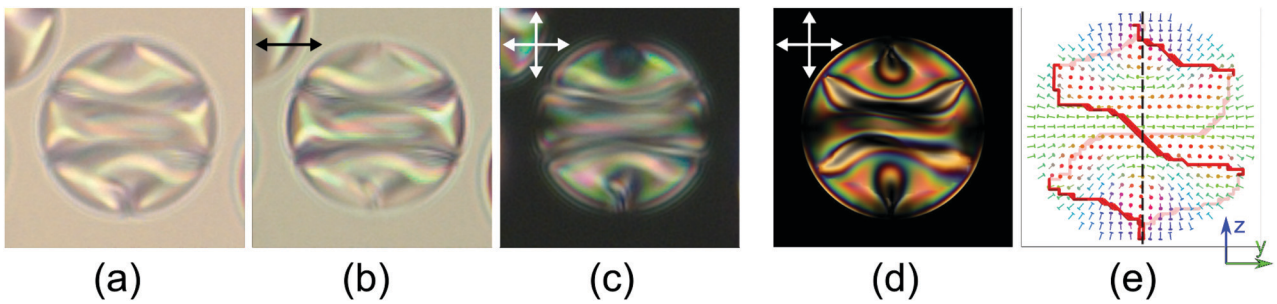

Fig. 5 Optical textures and director distributions of a 17 μm droplet ($N_0 = 6.2$) having the layer-like (**L**) structure. Microphotographs are taken in unpolarized light (a), at without analyzer (b), and in crossed polarizers (c). The simulated cross-polarized images (d) and corresponding director distributions in the central cross-section (e). The bipolar axis lies in the plane of the film. The polarizer is aligned perpendicularly to the bipolar axis. The thick red line indicates the twisted loop defect near the surface.

The structure transition from **R** to **tR** at N_0 = 1.3 shows gradual changes of all free energy terms and should be considered as a second order transition as follows from the analysis of the derivatives of splay, twist and bend elasticity energies with respect to the helicity parameter (see the dashed line in Fig. 6(b)). The transition occurs at the point where the partial compensation of twist deformation by splay and bend deformations leads to the decrease of the overall free energy of the system. With increasing helicity parameter N_0, the structure undergoes greater twist deformation, and the point defect shifts towards the droplet surface. However, the limited capacity of these changes with growing helicity makes the twisted radial structure energetically unfavorable at $N_0 \geq 3.2$.

At N_0 = 3.2, the transition from twisted radial to toron-like structures occurs. Both the splay and twist deformation energy terms abruptly decrease at the cost of the emergence of a circular linear disclination near the surface of the droplet. Thus, the transition is classified as first order (solid vertical line in Fig. 6(b)). The toron-like structure exhibits almost no changes with increasing N_0, resulting in almost flat plots of F_{splay}, F_{bend} and F_{def} between N_0 = 3.2 and 5.3. At N_0 = 5.3 the first order structure transition from the toron-like to the intermediate structure ($\mathbf{L}_0$) compensates the rising F_{twist} by twisting the circular defect. For other LC materials with different ratios between splay, twist and bend elastic constants, this structure may or may not occur (see Fig. S8, ESI†).

Finally, the layer-like (**L**) structure becomes the most energetically favorable at $N_0 \geq 5.8$ due to the much larger area of regular cholesteric layers in the central part of the droplet. As shown in Fig. 6(b), in the layer-like structure, unlike in the other structures, F_{def} grows very sharply with increasing N_0, while F_{twist} increases almost linearly with the increase of N_0. It makes this type of structure the most preferable at large droplet sizes. The transition from the intermediate ($\mathbf{L}_0$) to the layer-like (**L**) structure is also a first order transition.

The number turns of the director at the droplet diameter increases up to $N \cong 1.8$ and more in the structures with a bipolar distribution of the helix axis (Fig. 5) formed at $N_0 \geq 4.7$. As the droplet diameter (N_0) increases, the value of N gradually rises and $N \cong N_0$ for $N_0 \geq 10$ [57] as opposed to the structures with point defects and the toron-like configurations. For the studied system the characteristic range of values within which all the four configurations appear (see Fig. 6 (shaded region)) is $4.7 \leq N_0 \leq 5.4$. This fact clearly demonstrates a good capability of the cholesteric liquid crystal with homeotropic anchoring to form meta-stable configurations. For a long time their existence was conditioned by the availability of topological defects and different symmetry of the director field and of the helix axis. For example, the structures with point defects, the toron-like configuration and the structure with a bipolar distribution of the helix axis have an equivalent, from a topological point of view, singular defect. For this reason, the structure with a point defect can transform into the structure with a circular one.

It should be noted that a transition of a point defect into a circular one is observed in nematic droplets under an electric (magnetic) field[46,65,66] or upon a change of the dimensional parameters of the droplets.[59,67] As was shown in ref. 67, the transition between configurations is sharp and depends on the ratio of the droplet diameter, the elastic constants and the anchoring energy. A wide N_0 range (2.9–5.4, see Fig. 6a) for the structures with the point and linear defects in cholesterics can be explained by the cardinally differing helix axis distribution. Consequently, a change of topological defect type must be accompanied by a noticeable modification of the structure all over the bulk, which explains the existence of rather high energy barriers between the states. An analogous situation is observed for the pair of the toron-like configuration and the structure with a bipolar distribution of the helix axis. Both structures include linear defects, which makes a smooth transformation of one structure into another possible. However, such a transition should be accompanied by a considerable transformation of the director field, which has initially cylindrical symmetry, into a lower-symmetry structure. It specifies the existence of a potential barrier for the transition between these structures. The existence of stable and meta-stable intermediate states combining the features of both structures (Fig. 4) indicates a complex character of the potential barriers between them.

4 Conclusions

The orientational droplet structures of cholesteric liquid crystals under homeotropic anchoring obtained by the phase separation method have been experimentally studied. It has been shown that five distinctive structures are formed in cholesteric droplets upon changing the helicity parameter in the $0 < N_0 \leq 7$ range. At $N_0 < 1.1$ only an untwisted radial structure with a point defect in the center is realized. At larger values of N_0 (i) a structure with a shifted point defect, (ii) a toron-like structure, (iii) an intermediate layer-like configuration, and (iiii) a normal layer-like structure are formed. All these configurations are characterized by the presence of a single singular topologic defect: a point bulk defect or a circular defect near the surface. Interestingly, the structures with two or more singular defects observed in emulsions[50–52] are not realized in the samples under study. Structures with linear defects are observed instead despite their energy excess over the energy of point defects. This appeared to be possible because of the formation of linear defects leading to a significant decrease of the other components of the elastic energy, and generally to a decrease of the total system energy. Such a conclusion is proved by the simulation results obtained by the methods of free energy minimization using the Frank elastic continuum approach with Monte-Carlo annealing optimization. A detailed analysis of the dependence of the free energy and its components on the relative helicity parameter demonstrates the presence of critical N_0 values, at which kinks and sharp jumps occur. Near these special N_0 values the structure kind transforms cardinally. Analysis shows all orientation structures observed in the experiment are formed under a gradual increase of the N_0 value.

As the helix pitch decreases (N_0 increases) the following sequence of structures can be observed: radial (**R**) – twisted

radial (**tR**) – toron-like (**T**) – intermediate layer-like ($\mathbf{L}_0$) – layer-like structure with a bipolar distribution of the helix pitch (**L**). Nevertheless, the presence of the 4.7–5.4 N_0 range in the experiment in Fig. 6a where the four structures can coexist means that the transition, for example, from twisted radial directly into the structure with a bipolar distribution of the helix axis and *vice versa* is possible. Moreover, in this range of N_0 the configurations formed in the droplets can be very sensitive to a change of the system parameters (anchoring energy, temperature, the ratio of the elastic constants of the LC *etc.*) or external factors (electric field). This fact should be studied in detail.

Conflicts of interest

There are no conflicts of interest to declare.

Acknowledgements

This work was supported by the Russian Foundation for Basic Research Project No. 19-53-52011 MNT_a. The research is carried out using the equipment of the shared research facilities of HPC computing resources at Lomonosov Moscow State University supported by the project RFMEFI62117X0011.

References

1 P. Oswald and P. Pieranski, *Nematic and cholesteric liquid crystals: concepts and physical properties illustrated by experiments*, Taylor & Francis, Boca Raton, 2005.
2 S. J. Woltman, G. D. Jay and G. P. Crawford, *Nat. Mater.*, 2007, **6**, 929–938.
3 S. J. Asshoff, S. Sukas, T. Yamaguchi, C. A. Hommersom, S. Le Gac and N. Katsonis, *Sci. Rep.*, 2015, **5**, 14183.
4 Y. Geng, J. Noh, I. Drevensek-Olenik, R. Rupp, G. Lenzini and J. P. F. Lagerwall, *Sci. Rep.*, 2016, **6**, 26840.
5 T. Skyrme, *Nucl. Phys.*, 1962, **31**, 556–569.
6 P. Kurioz, M. Kralj, B. S. Murray, C. Rosenblatt and S. Kralj, *Beilstein J. Nanotechnol.*, 2018, **9**, 109–118.
7 P. J. Ackerman and I. I. Smalyukh, *Phys. Rev. X*, 2017, **7**, 011006.
8 M. Nakata, G. Zanchetta, B. D. Chapman, C. D. Jones, J. O. Cross, R. Pindak, T. Bellini and N. A. Clark, *Science*, 2007, **318**, 1276–1279.
9 L. Tran, M. O. Lavrentovich, G. Durey, A. Darmon, M. F. Haase, N. Li, D. Lee, K. J. Stebe, R. D. Kamien and T. Lopez-Leon, *Phys. Rev. X*, 2017, **7**, 041029.
10 D. A. Beller, T. Machon, S. Copar, D. M. Sussman, G. P. Alexander, R. D. Kamien and R. A. Mosna, *Phys. Rev. X*, 2014, **4**, 031050.
11 S. V. Belyaev and L. M. Blinov, *JETP*, 1976, **43**, 96–99.
12 B. Ya. Zel'dovich and N. V. Tabiryan, *JETP Lett.*, 1981, **34**, 406–408.
13 W. J. A. Goossens, *J. Phys.*, 1982, **43**, 1469–1474.
14 P. E. Cladis and M. Kleman, *Mol. Cryst. Liq. Cryst.*, 1972, **16**, 1–20.
15 J. Baudry, M. Brazovskaia, L. Lejcek, P. Oswald and S. Pirkl, *Liq. Cryst.*, 1996, **21**, 893–901.
16 L.-L. Ma, S.-S. Li, W.-S. Li, W. Ji, B. Luo, Z.-G. Zheng, Z.-P. Cai, V. Chigrinov, Y.-Q. Lu, W. Hu and L.-J. Chen, *Adv. Opt. Mater.*, 2015, **3**, 1691–1696.
17 C.-H. Lin, R.-H. Chiang, S.-H. Liu, C.-T. Kuo and C.-Y. Huang, *Opt. Express*, 2012, **20**, 26837.
18 T. Beica, S. Frunza, R. Moldovan, M. Giurgea and M. Tintaru, *Liq. Cryst.*, 1993, **13**, 127–138.
19 R. S. Zola, L. R. Evangelista, Y.-C. Yang and D.-K. Yang, *Phys. Rev. Lett.*, 2013, **110**, 057801.
20 D. Subacius, S. V. Shiyanovskii, P. Bos and O. D. Lavrentovich, *Appl. Phys. Lett.*, 1997, **71**, 3323–3325.
21 B. I. Senyuk, I. I. Smalyukh and O. D. Lavrentovich, *Opt. Lett.*, 2005, **30**, 349.
22 M. Press and A. Arrott, *J. Phys.*, 1976, **37**, 387–395.
23 W. E. L. Haas and J. E. Adams, *Appl. Phys. Lett.*, 1974, **25**, 535–537.
24 A. N. Bogdanov and A. A. Shestakov, *J. Exp. Theor. Phys.*, 1998, **86**, 911–923.
25 P. Oswald, J. Baudry and S. Pirkl, *Phys. Rep.*, 2000, **337**, 67–96.
26 A. O. Leonov, I. E. Dragunov, U. K. Rossler and A. N. Bogdanov, *Phys. Rev. E: Stat., Nonlinear, Soft Matter Phys.*, 2014, **90**, 042502.
27 J. Baudry, S. Pirkl and P. Oswald, *Phys. Rev. E: Stat. Phys., Plasmas, Fluids, Relat. Interdiscip. Top.*, 1999, **59**, 5562–5571.
28 I. I. Smalyukh, Y. Lansac, N. A. Clark and R. P. Trivedi, *Nat. Mater.*, 2010, **9**, 139–145.
29 P. J. Ackerman, R. P. Trivedi, B. Senyuk, J. van de Lagemaat and I. I. Smalyukh, *Phys. Rev. E: Stat., Nonlinear, Soft Matter Phys.*, 2014, **90**, 012505.
30 W. E. L. Haas and J. E. Adams, *Appl. Phys. Lett.*, 1974, **25**, 263–264.
31 P. J. Ackerman, Z. Qi and I. I. Smalyukh, *Phys. Rev. E: Stat., Nonlinear, Soft Matter Phys.*, 2012, **86**, 021703.
32 P. J. Ackerman, Z. Qi, Y. Lin, C. W. Twombly, M. J. Laviada, Y. Lansac and I. I. Smalyukh, *Sci. Rep.*, 2012, **2**, 414.
33 A. Varanytsia, G. Posnjak, U. Mur, V. Joshi, K. Darrah, I. Musevic, S. Copar and L.-C. Chien, *Sci. Rep.*, 2017, **7**, 16149.
34 H.-S. Kitzerow, *Liq. Cryst.*, 1994, **16**, 1–31.
35 Y. Geng, J.-H. Jang, K.-G. Noh, J. Noh, J. P. F. Lagerwall and S.-Y. Park, *Adv. Opt. Mater.*, 2018, **6**, 1700923.
36 M. Humar and I. Musevic, *Opt. Exp.*, 2010, **18**, 26995–27003.
37 G. Cipparrone, A. Mazzulla, A. Pane, R. J. Hernandez and R. Bartolino, *Adv. Mater.*, 2011, **23**, 5773–5778.
38 G. Tkachenko and E. Brasselet, *Nat. Commun.*, 2014, **5**, 3577.
39 J. Yoshioka and F. Araoka, *Nat. Commun.*, 2018, **9**, 432.
40 J. Yoshioka, F. Ito, Y. Suzuki, H. Takahashi, H. Takizawa and Y. Tabe, *Soft Matter*, 2014, **10**, 5869.
41 T. Yamamoto and M. Sano, *Soft Matter*, 2017, **13**, 3328–3333.
42 F. Xu and P. P. Crooker, *Phys. Rev. E: Stat. Phys., Plasmas, Fluids, Relat. Interdiscip. Top.*, 1997, **56**, 6853–6860.
43 J. Bezic and S. Zumer, *Liq. Cryst.*, 1992, **11**, 593–619.
44 Y. Zhou, E. Bukusoglu, J. A. Martinez-Gonzalez, M. Rahimi, T. F. Roberts, R. Zhang, X. Wang, N. L. Abbott and J. J. de Pablo, *ACS Nano*, 2016, **10**, 6484–6490.
45 Y. Bouligand and F. Livolant, *J. Phys.*, 1984, **45**, 1899–1923.
46 S. Candau, P. Le Roy and F. Debeauvais, *Mol. Cryst. Liq. Cryst.*, 1973, **23**, 283–297.

47 D. Sec, T. Porenta, M. Ravnik and S. Zumer, *Soft Matter*, 2012, **8**, 11982.
48 A. Darmon, M. Benzaquen, D. Sec, S. Copar, O. Dauchot and T. Lopez-Leon, *Proc. Natl. Acad. Sci. U. S. A.*, 2016, **113**, 9469–9474.
49 A. Darmon, M. Benzaquen, S. Copar, O. Dauchot and T. Lopez-Leon, *Soft Matter*, 2016, **12**, 9280–9288.
50 G. Posnjak, S. Copar and I. Musevic, *Sci. Rep.*, 2016, **6**, 26361.
51 G. Posnjak, S. Copar and I. Musevic, *Nat. Commun.*, 2017, **8**, 14594.
52 J. Pollard, G. Posnjak, S. Copar, I. Musevic and G. P. Alexander, *Phys. Rev. X*, 2019, **9**, 021004.
53 H.-S. Kitzerow and P. P. Crooker, *Liq. Cryst.*, 1993, **13**, 31–43.
54 M. N. Krakhalev, A. P. Gardymova, O. O. Prishchepa, V. Y. Rudyak, A. V. Emelyanenko, J.-H. Liu and V. Y. Zyryanov, *Sci. Rep.*, 2017, **7**, 14582.
55 D. Sec, S. Copar and S. Zumer, *Nat. Commun.*, 2014, **5**, 3057.
56 J. Pierron, V. Tournier-Lasserve, P. Sopena, A. Boudet, P. Sixou and M. Mitov, *J. Phys. II*, 1995, **5**, 1635–1647.
57 M. N. Krakhalev, A. P. Gardymova, A. V. Emelyanenko, J.-H. Liu and V. Y. Zyryanov, *JETP Lett.*, 2017, **105**, 51–54.
58 P. S. Drzaic, *Liquid crystal dispersions*, World Scientific, Singapore, 1995.
59 V. Y. Rudyak, A. V. Emelyanenko and V. A. Loiko, *Phys. Rev. E: Stat., Nonlinear, Soft Matter Phys.*, 2013, **88**, 052501.
60 V. Y. Rudyak, M. N. Krakhalev, V. S. Sutormin, O. O. Prishchepa, V. Y. Zyryanov, J.-H. Liu, A. V. Emelyanenko and A. R. Khokhlov, *Phys. Rev. E*, 2017, **96**, 052701.
61 S. A. Shvetsov, V. Y. Rudyak, A. V. Emelyanenko, N. I. Boiko, Y.-S. Zhang, J.-H. Liu and A. R. Khokhlov, *J. Mol. Liq.*, 2018, **267**, 222–228.
62 R. Ondris-Crawford, E. P. Boyko, B. G. Wagner, J. H. Erdmann, S. Zumer and J. W. Doane, *J. Appl. Phys.*, 1991, **69**, 6380–6386.
63 J. Li, C.-H. Wen, S. Gauza, R. Lu and S.-T. Wu, *J. Disp. Technol.*, 2005, **1**, 51–61.
64 T. Orlova, S. J. Asshoff, T. Yamaguchi, N. Katsonis and E. Brasselet, *Nat. Commun.*, 2015, **6**, 7603.
65 A. V. Koval'chuk, M. V. Kurik, O. D. Lavrentovich and V. V. Sergan, *JETP*, 1988, **67**, 1065–1073.
66 V. G. Bodnar, O. D. Lavrentovich and V. M. Pergamenshchik, *JETP*, 1992, **74**, 60–67.
67 J. H. Erdmann, S. Zumer and J. W. Doane, *Phys. Rev. Lett.*, 1990, **64**, 1907–1910.